We are IntechOpen, the world's leading publisher of Open Access books
Built by scientists, for scientists

6,900
Open access books available

185,000
International authors and editors

200M
Downloads

Our authors are among the

154
Countries delivered to

TOP 1%
most cited scientists

12.2%
Contributors from top 500 universities

WEB OF SCIENCE™

Selection of our books indexed in the Book Citation Index in Web of Science™ Core Collection (BKCI)

Interested in publishing with us?
Contact book.department@intechopen.com

Numbers displayed above are based on latest data collected.
For more information visit www.intechopen.com

Chapter

Self-Assembly of Nanoparticles Decorated by Liquid Crystalline Groups: Computer Simulations

Jaroslav Ilnytskyi

Abstract

We present the results of the computer simulations for the self-assembly of decorated nanoparticles. The models are rather generic and comprise a central core and a shell of ligands containing terminal liquid crystalline group, including the case of the azobenzene chromophores. The simulations are performed using the coarse-grained molecular dynamics with the effective soft-core interparticle interaction potentials obtained from the atomistic simulations. The discussion is centred around the set of the self-assembled morphologies in a melt of 100–200 of such decorated nanoparticles obtained upon the change of the temperature, surface density of ligands, the type of the terminal group attachment, as well as the prediction of the possibility of photo-assisted self-assembly of the nanoparticles decorated by the azobenzene chromophores.

Keywords: self-assembly, nanoparticles, molecular dynamics, azobenzene

1. Introduction

Nanoparticles gained extended research and technological focus due to their unique optical, electronic, magnetic and chemical properties [1]. Applications include: medical diagnostics, drug delivery, cancer therapy, nanoelectronics and information storage, sensors, (photo)catalysis, surface coatings [2]. Self-assembly of nanoparticles are in a core of many advanced materials developments coining the term ‘nanoarchitectonics’ [3]. Self-assembly process becomes more controllable by decoration of nanoparticles with functional ligands. Good example is decorated nanoparticles (DNP) coated by the liquid crystalline (LC) ligands [4–9] that are considered in this chapter.

The structure of the self-assembled morphology depends on: (i) the details of molecular architecture, and (ii) external conditions. The group (i) includes the type of the core nanoparticle (metal/non-metal, magnetic/non-magnetic, etc.); grafting density, length, flexibility and chemical details of ligands; number and type of functionalisation groups, etc. The group (ii) includes the temperature, pressure/density, the presence of surfaces and external fields. Prediction of symmetry/structure/properties of the self-assembled morphology, especially by means of theoretical methods, is quite problematic.

Computer simulations are of great aid here, as these incorporate the relevant details of molecular architecture and tackle statistical behaviour of many-particle

systems under specified external conditions. This approach faces a difficulty in terms of a wide span of the time- and length-scales typical for the supramolecular self-assembly. In particular, if more chemistry-specific details are taken into account—then relatively small system sizes and short simulation times can be covered. A good compromise can be achieved by using elements of a multiscale approach [10, 11], which builds a coarse-grained model based on the simulation data of a more chemically-detailed model. A coarse-grained model is of rather generic type capturing essential physical details of the atomistic system and allowing to reach required time- and length-scales of a self-assembly [12, 13]. Due to inevitable loss of specific chemical details, the comparison with particular chemical realisations is performed on a high level only—via the structure of observed morphologies and via the temperature- or density-driven phase transitions between them.

We cover the details of a coarse-grained modelling and self-assembly of DNPs containing LC groups (including the case of azobenzene chromophores). Computer simulations are performed via the molecular dynamics simulation combined with stochastic photoisomerisation events (in the case of azobenzene chromophores). As the result, this type of modelling enables to consider the role of grafting density and type of LC group attachment, as well as the role of the temperature and external fields (including illumination) on the process of self-assembly. Section 2 contains modelling and simulation details, in Section 3 we consider temperature related effects of the self-assembly, Section 4 covers the role of the details of molecular architecture, in Section 5 we cover the photo-aided self-assembly of DNPs containing azobenzene chromophores.

2. Modelling and simulation details

To study self-assembly of DNPs we use coarse-grained modelling, where relevant groups of atoms are replaced by single beads that interact via soft-core potentials. The model DNP is represented schematically in left frame of **Figure 1**. It is built from a central core and N_{ch} ligands that are free to surf on its surface. Each ligand is terminated by a LC group. The model equally may represent a generation three carbosilane dendrimer [14, 15].

The model contains spherical beads (designated thereafter as 'sp') and the spherocylinder ('sc') ones that mimic LC groups. The sphere-sphere interaction is soft repulsive of quadratic form

$$V_{ij}^{\mathrm{sp-sp}} = \begin{cases} U_{\max}^{\mathrm{sp-sp}}\left(1 - r_{ij}^{*}\right)^{2}, & r_{ij}^{*} < 1 \\ 0, & r_{ij}^{*} \geq 1, \end{cases} \qquad (1)$$

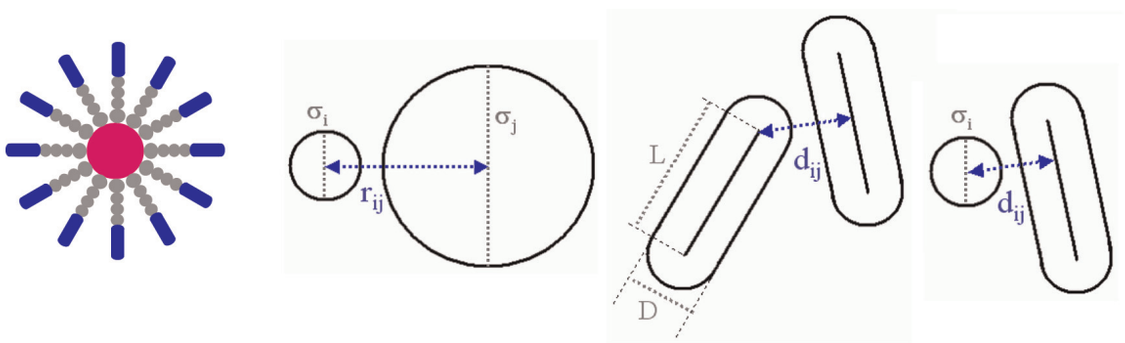

Figure 1.
Model DNP (left frame). Definition of sizes and distances for pairs of interacting beads (right frame).

where $r_{ij}^* = r_{ij}/\sigma_{ij}$ is scaled distance between centres of ith and jth sphere and mixing rules $\sigma_{ij} = (\sigma_i + \sigma_j)/2$ are implied (see right frame of **Figure 1**). $U_{\max}^{\text{sp-sp}}$ is the same for all interacting spheres.

Spherocylinders are of breadth D and of elongation L/D and interact via the soft anisotropic potential of Lintuvuori and Wilson [16]:

$$V_{ij}^{\text{sc-sc}} = \begin{cases} U_{\max}^{\text{sc-sc}}\left(1 - d_{ij}^*\right)^2, & d_{ij}^* < 1 \\ U_{\max}^{\text{sc-sc}}\left(1 - d_{ij}^*\right)^2 - U_{attr}^*\left(\hat{r}_{ij}, \hat{e}_i, \hat{e}_j\right)\left(1 - d_{ij}^*\right)^4 + \epsilon^*, & 1 \le d_{ij}^* < d_c^* \\ 0, & d_{ij}^* > d_c^*, \end{cases} \quad (2)$$

where $d_{ij}^* = d_{ij}/D$ is the dimensionless nearest distance between the cores of spherocylinders (see right frame of **Figure 1**), d_c^* is the orientation dependent cutoff. Attractive interaction has the form:

$$U_{\text{attr}}^*\left(\hat{r}_{ij}, \hat{e}_i, \hat{e}_j\right) = U_{\text{attr}}^* - \left[5\epsilon_1 P_2\left(\hat{e}_i \cdot \hat{e}_j\right) + 5\epsilon_2\left(P_2\left(\hat{r}_{ij} \cdot \hat{e}_i\right) + P_2\left(\hat{r}_{ij} \cdot \hat{e}_j\right)\right)\right] \quad (3)$$

and depend on orientations $\hat{e}_i$ and $\hat{e}_j$ of the long axes of spherocylinders and the unit vector $\hat{r}_{ij}$ that connects their centres [16]. $P_2(x) = 1/2(3x^2 - 1)$ is the second Legendre polynomial, energy parameters U_{attr}^*, ϵ_1 and ϵ_2 are given below. The inclusion of the attractive contribution in Eq. (2) shifts the region for the LC stability towards smaller elongations $L/D \sim 3$ compared to the case of purely repulsive interactions, where, typically, $L/D \sim 6 - 8$ [14].

Mixed nonbonded interactions are evaluated in a similar way to Eq. (1)

$$V_{ij}^{\text{sp-sc}} = \begin{cases} U_{\max}^{\text{sp-sc}}\left(1 - d_{ij}^*\right)^2, & d_{ij}^* < 1 \\ 0, & d_{ij}^* \ge 1, \end{cases} \quad (4)$$

where $d_{ij}^* = d_{ij}/\sigma_{ij}$ is a dimensionless distance between the centre of the ith sphere and the core of the jth spherocylinder (see right frame of **Figure 1**), with the scaling factor $\sigma_{ij} = (\sigma_i + D)/2$.

Intramolecular interactions for the model include bond and angle interactions terms

$$V_{\text{bonded}} = \sum_{i=1}^{N_b} k_b\left(l_i - l_0^k\right)^2 + \sum_{i=1}^{N_a} k_a\left(\theta_{ijk} - \theta_0\right)^2, \quad (5)$$

where l_i is the instantaneous bond length, $\left\{l_0^k\right\}$ is the set of effective bond lengths. Ligands stiffness is adjustable via the magnitude of k_a, and θ_0 is set equal to π.

The force-field parameters are based on the coarse-graining of the LC dendrimer first performed and described in detail in Ref. [14]. Bulk behaviour of such macromolecules are very similar to that of the DNPs [17]. The soft-core diameters of spherical beads are: $\sigma = 21.37$, 6.23 and 4.59 Å for the core, first ligand bead and the following ligans beads, respectively. Their respective masses: $62.44 \cdot 10^{-25}$, $2.20 \cdot 10^{-25}$ and $0.70 \cdot 10^{-25}$ kg. LC beads dimension are $D = 3.74$ Å, $L/D = 3$, their mass is $3.94 \cdot 10^{-25}$ kg and the moment of inertia: $6.00 \cdot 10^{-24}$ kg. The energy parameters $U_{\max}^{\text{sp-sc}}$, $U_{\max}^{\text{sp-sc}}$ and $U_{\max}^{\text{sp-sc}}$ are all equal to $70 \cdot 10^{-20}$ J. LC-LC specific energy parameters are $U_{\text{attr}}^* = 1500 \cdot 10^{-20}$, $\epsilon_1 = 120 \cdot 10^{-20}$ and $\epsilon_2 = -120 \cdot 10^{-20}$ J. The bond

lengths are: 14.9, 3.60 and 3.62 Å between the core-first spacer bead, first-second spacer bead and between following spacer beads, respectively. The spherocylinder is attached to the centre of its nearest spherical cap with the bond length of 2.98 Å. The bond interaction spring constant is $50 \cdot 10^{-20}$ J for all bonds. The pseudo-valent angle spring constant is $20 \cdot 10^{-20}$ J.

The simulations are carried out with the GBMOLDD program extended to the case of the $NP_xP_yP_zT$ ensemble [18]. We use a single Nóse-Hoover thermostat in most cases for both translational and rotational degrees of freedom. In quenching or rapid heating runs the velocity rescaling was used instead. The timestep $\Delta t \sim 20$ fs was used for velocity rescaling runs, whereas smaller timesteps $\Delta t \sim 10 - 15$ fs was required for the runs with the thermostat. To control pressure three barostats are used [18].

3. Temperature driven morphology changes

In this section we consider temperature driven transitions between ordered and disordered morphologies observed in the DNPs melt. The experimental evidence for such transitions are found in Refs. [4–9, 17] and indicate a close relation between the average DNPs shape and the type of the ordered morphology. Therefore, we attempt to steer the self-assembly towards particular morphology by influencing the DNPs shape. To do so we impose the orientation field of a given symmetry, which acts on the LC beads. It is introduced via the following energy term

$$U_{\text{rot}} = -F(\mathbf{e}_i \cdot \mathbf{i})^2, \tag{6}$$

where $\mathbf{e}_i$ is the orientation of ith LC bead, $\mathbf{i}$ is the direction of the field, whereas field strength F provides either uniaxial ($F>0$) or planar ($F<0$) preferred orientation of the LC beads. In turn, in these cases we expect, respectively, rod-like or disc-like conformations of DNPs.

The case of the uniaxial field is considered first. Applied to the isotropic morphology of 100 DNPs in bulk using the $NP_xP_yP_zT$ ensemble at $P = 50$ atm and $T = 520$ K, the field of the strength $F = 2 \cdot 10^{-20}$ J and with $\mathbf{i}$ collinear to the Z-axis, it induces formation of a monodomain smectic A (Sm_A) morphology. It was studied then with the field switched off and the melt equilibrated for $20 - 40$ ns at selected temperatures within a range of $T \in [350\text{ K}, 650\text{ K}]$. Its appearance is shown in **Figure 2** indicating a lamellar structure with alternating layers of cores, ligand chains and LC beads (shown in left frame), in agreement with the experimental studies [5, 17]. The two-dimensional arrangement within layers is shown in the right frame.

We examined spatial distribution of the DNPs cores next. The form of their radial distribution function $g(r)$ is similar within a range of $T = 350 - 470$ K indicating two maxima: one at $r \sim 27$ Å for the short-range order of cores within each layer, and another at $r \sim 65$ Å, related to the interlayer distance (see, **Figure 3**, left frame). These characteristic distances are model dependent and can be examined by evaluting pair distribution functions $g_\text{z}(r)$ and $g_{\text{xy}}(r)$. The former yields an interlayer distance at ~ 59 Å (**Figure 3**, right frame). The latter indicates some degree of local (but not long-ranged) positional order within the layers (**Figure 3**, middle frame), characteristic of a 2D liquid. Therefore the phase is identified as the smectic A (Sm_A) [5, 17].

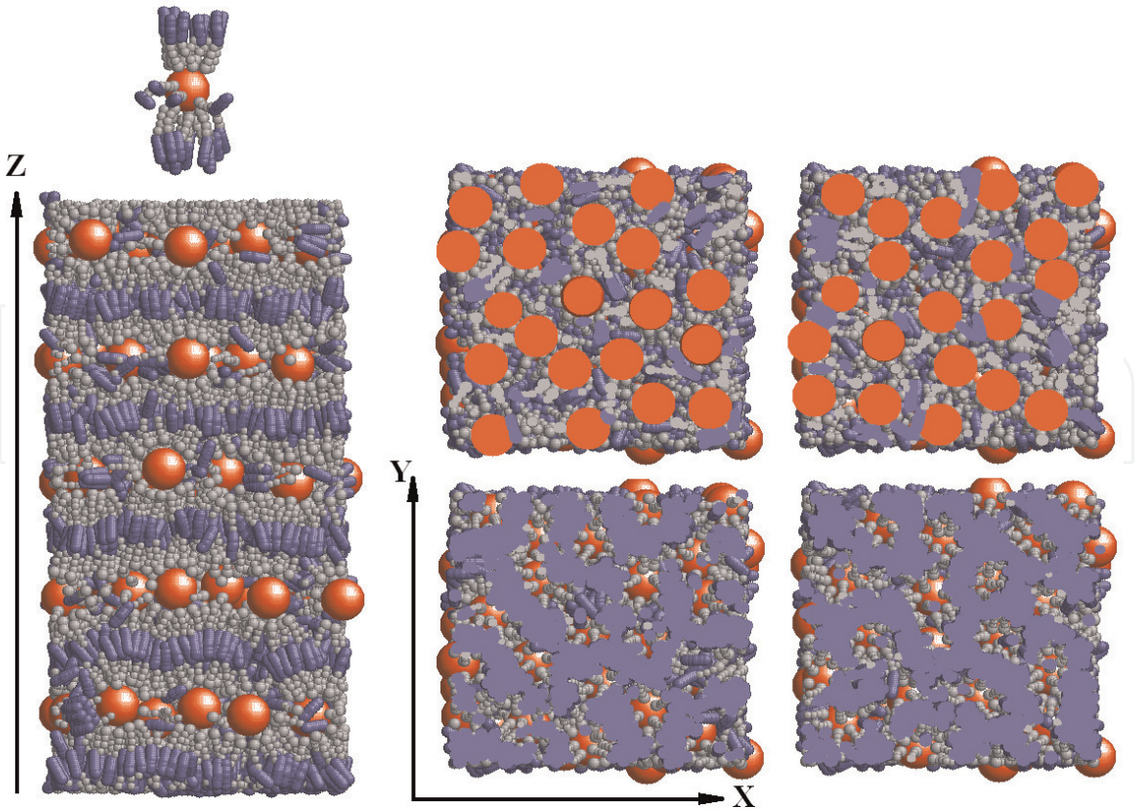

Figure 2.
Snapshots of the Sm_A phase at $T = 470\,K$ including typical rod-like molecular conformation.

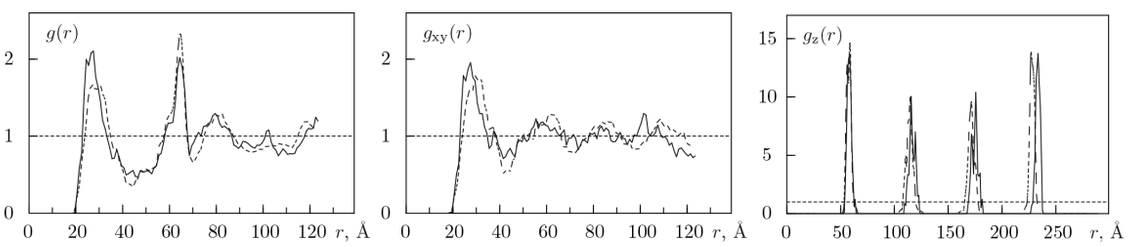

Figure 3.
Radial distribution functions $g(r)$ (left frame), $g_{xy}(r)$ (middle frame) and $g_z(r)$ (right frame) for the DNPs cores in the Sm_A phase at $T = 350\,K$ (solid lines) and at $T = 470\,K$ (dashed lines).

Application of a field with a planar symmetry ($F < 0$) along the Z axis, leads to the formation of a columnar (Col) morphology. The defect-free monodomain sample is achieved by using the field of a moderate magnitude, $F = -2 \cdot 10^{-20}$ J applied to the isotropic melt at $P = 50$ atm and $T \sim 520$ K. It was subsequently studied in a series of runs at the temperatures in the range $T \in [350\,\text{K}, 650\,\text{K}]$ and is shown at $T =$ 490 K in **Figure 4**. It displays disc-like DNPs stacked into columns, whereas the columns theirselves are arranged hexagonally, in accordance with the experimental observations [4].

The structure of Col phase is analysed via the pair distribution functions, shown in **Figure 5**. The hexagonal arrangement of columns is clearly indicated in the form of $g_{\text{xy}}(r)$, while the peaks in $g_{\text{z}}(r)$ allow the distance between dendritic cores within a column to be estimated as $\sim 18\,\text{Å}$ for the Col phase at $T = 350$ K and ~20 Å at $T = 490$ K.

Upon heating up, both ordered morphologies, Sm_A and Col, undergo transitions to the spatially disordered phase as monitored via the order parameter S_N of

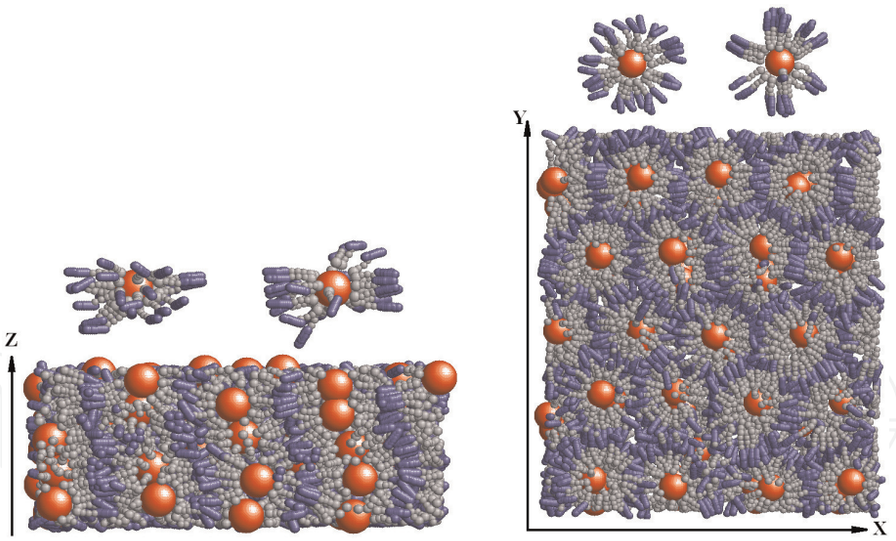

Figure 4.
Snapshots of the Col phase at $T = 490\,K$ including typical disc-like molecular conformation.

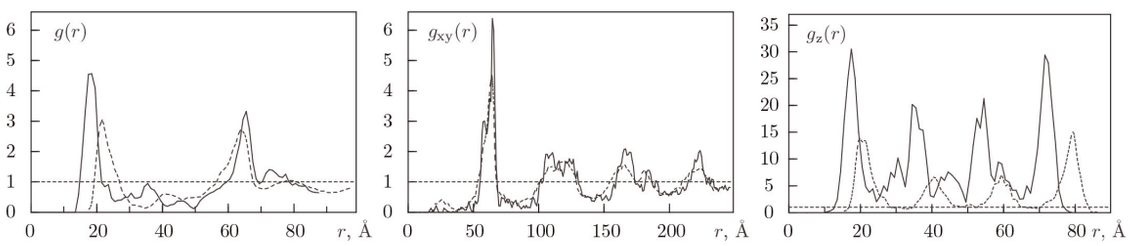

Figure 5.
Radial distribution functions $g(r)$ (left frame), $g_{xy}(r)$ (middle frame) and $g_z(r)$ (right frame) for the DNPs cores in the Col phase at $T = 350\,K$ (solid lines) and at $T = 470\,K$ (dashed lines).

mesogens with respect to the axis **i** (nematic director for the Sm_A and the columns vector for the Col symmetry)

$$S_N = \langle P_2(\mathbf{e}_i \cdot \mathbf{i}) \rangle, \tag{7}$$

where $P_2(x)$ is the second Legendre polynomial and averaging is performed on all mesogens in a melt. As far as in this section the field is always collinear to the Z-axis, the notation S_z is also used. Shape asymmetry of DNPs, a, is obtained from the components of the gyration tensor $G_{\alpha\beta}$

$$G_{\alpha\beta} = \frac{1}{N}\sum_{i=1}^{N}(r_{i,\alpha} - R_\alpha)(r_{i,\beta} - R_\beta), \quad a = \frac{1}{R_g^2}\left[G_{zz} - \frac{G_{xx} + G_{yy}}{2}\right], \tag{8}$$

where α, β stay for the Cartesian axes, $r_{i,\alpha}$ and R_α are the coordinates of the individual beads and of the DNP's centre of mass, respectively, $R_g^2 = \sum_{\alpha\alpha} G_{\alpha\alpha}$ is the squared radius of gyration. Each spherocylinder bead is replaced by a line of four centres. The shape anisotropy a is positive for the prolate shape and negative for the oblate one.

S_z, a and the system density ρ are all shown as the functions of the temperature in **Figure 6** for both Sm_A (left frame) and Col (right frame) morphologies. At lower temperatures both S_z and a are non-zero, indicating the Sm_A and Col phases and quantifying the amount of orientation order and DNPs shape asymmetry at each temperature. Transition to the disordered isotropic morphology occurs at about $T = 490 - 500\,K$, where both S_z and a simultaneously turn to zero.

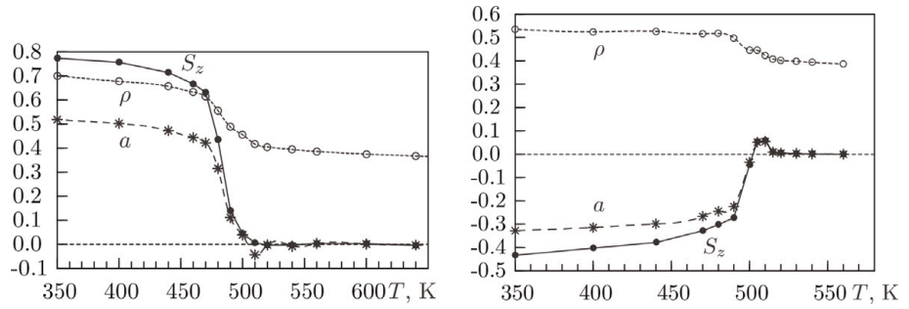

Figure 6.
Evolution of the density, shape asymmetry and the order parameter at the Sm_A-I and Col-I phase transitions.

The simulations reproduce a strong link between the shape of a DNPs and the type of bulk morphology, as previously observed experimentally [4, 17]. In particular, rod shapes are compatible with the Sm_A symmetry (**Figure 2**), discotic shapes are compatible with Col symmetry (**Figure 4**) and an spherical molecular shape is found in an isotropic state. This confirms the validity of the present model, which catches main features of the DNPs bulk assembly. The prolate-to-isotropic and oblate-to-isotropic shape transition occur simultaneously with vanishing the respective order parameter, as shown in **Figure 6**. The DNPs demonstrate shape bistability leading to the possibility to observe different symmetries at the same thermodynamics condition. As will be shown in the following section, this feature is dependent of the density of ligands defined via N_{ch}.

4. The role of the details of the molecular architecture

4.1 Variation of a grafting density

In Section 3 the number of ligands in DNPs was kept fixed at $N_{ch} = 32$. The decoration density, however, can change the shape of the supermolecule leading to different types of self-organised structure [4, 6, 17]. On the first sight, the most favourable conformation at any N_{ch} could be estimated from space-filling considerations and then the type of self-assembled morphology could be predicted. This was attempted in [19] but showed that the temperature effects also plays a crucial role and the symmetry of the self-assembled morphology at each conditions is the result of a delicate balance between the enthalpic and entropic contributions to the free energy.

Based on experimental findings [5, 8, 9, 17, 20], we expect to observe the sequence of Sm_A, Col and cubic morphologies upon the increase of N_{ch}. For each N_{ch}, we performed aided self-assembly runs of duration 20 ns at $T = 520$K with the timestep of 20 fs in the $NP_xP_yP_zT$ ensemble. Both uniaxial and planar fields were used. Then, the field was switched off and the system was equilibrated at $T = 450$ K, about 50 K below the transition. Besides these, the spontaneous self-assembly runs were performed, too. In the latter, the temperature of the melt was reduced linearly from $T = 500$K down to 450 K during first 20 ns (cooling rate is 2.5 K/ns), followed by another run for 20 ns at fixed $T = 450$K. As the result, relatively defect-free smectic layers are found for the cases of $N_{ch} = 12$ and $N_{ch} = 20$ only, whereas at $N_{ch} \leq 24$ we obtained polydomain layered structures with either one type of domains (of smectic or discotic type) or a mixture of both. In the field-aided self-assembly the external field (6) was employed, similarly as described in

Section 3. Both runs with uniaxial ($F>0$) and planar ($F<0$) fields were undertaken for each case of the number of ligands N_{ch} being considered.

Due to a relatively small system size, firm identification of smectic and discotic domains turned to be quite problematic, the visual inspection indicates domains of just a few DNPs. Therefore, we opted to analyse the distribution of the DNPs shape asymmetries instead, assuming that each rod-shaped DNP is a part of a smectic domain and a disc-shaped one—of the discotic one, as demonstrated earlier in Section 1. To distinguish between two shapes, we introduce molecular 'roddicity' a_r (always positive) and molecular 'discoticity' a_d (always negative):

$$a_r = \frac{1}{R_g^2}\left[\lambda_{\max} - \frac{\lambda_{\text{med}} + \lambda_{\min}}{2}\right], \qquad a_d = \frac{1}{R_g^2}\left[\lambda_{\min} - \frac{\lambda_{\text{med}} + \lambda_{\max}}{2}\right], \tag{9}$$

for each DNP. Here $\lambda_{\max}$, λ_{med} and $\lambda_{\min}$ are the maximum, medium and minimum eigenvalues of the gyration tensor (8), respectively. If, for given DNP, $|a_r|>|a_d|$, then it is classified as a rod with the shape anisotropy $a' = a_r$, otherwise—as a disc with $a' = a_d$. At each time instance, the DNP melt splits into rods and discs subsystems, with their fractions termed as f_r and f_d, respectively.

The histograms for the distribution $p(a')$ are built over all the DNPs in the system averaged over time trajectory and are shown in **Figure 7** for selected values of N_{ch}. Both the cases of unaided (left frame) and field-aided self-assembly (middle and right frames) are displayed. In the case of spontaneous self-assembly, rods and discs always coexist and the distributions of their shape asymmetry are relatively broad. With the increase of N_{ch}, two maxima gradually merge into a spherulitic shape from both sides of $a' = 0$ (at about $N_{ch} = 64$ and higher). The histograms at the field-aided self-assembly are much narrower. In the case of uniaxial field, the discotic conformations are completely eliminated (except the case of $N_{ch} = 48$ where smectic phase is not observed any more), as these are incompatible with the 1D symmetry of the aiding field. In the case of planar filed, which has a 2D symmetry, the rod-like conformations are not eliminated and do appear within XY plane, and are, in fact, the dominant ones at smaller values of N_{ch}. With the increase of N_{ch} above 24 the disc-like conformations are dominating.

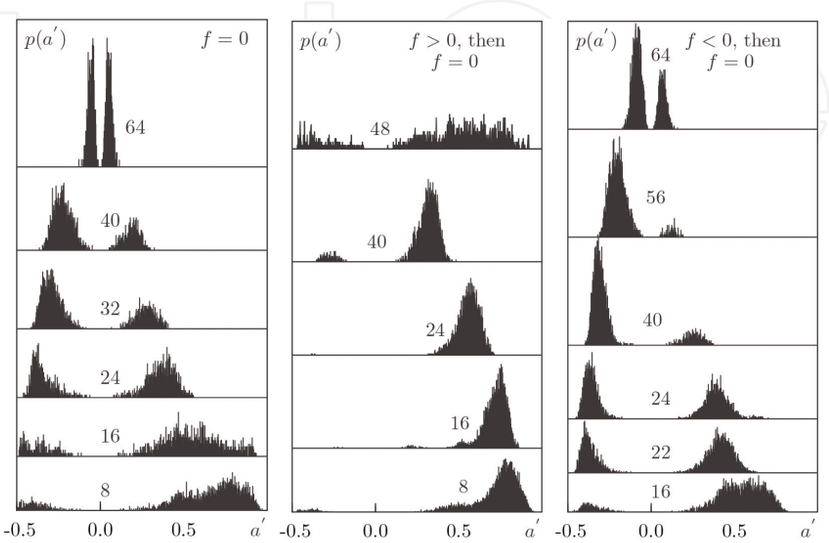

Figure 7.
Histograms for the distributions of shape anisotropy $p(a')$ at spontaneous self-assembly (left image), uniaxial field aided self-assembly (middle image) and planar field aided self-assembly (right image).

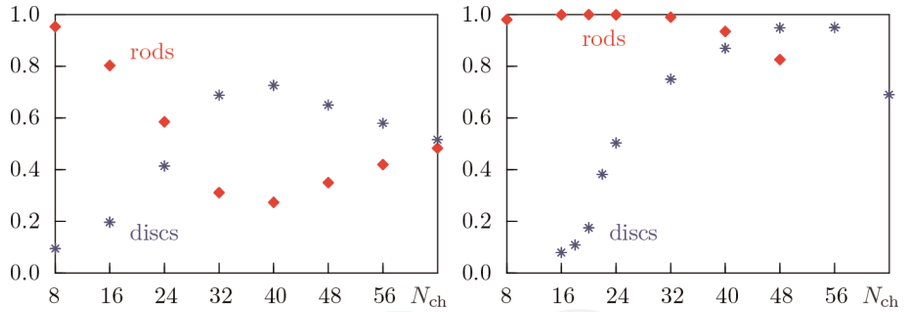

Figure 8.
Fraction of rods and discs for unaided self-assembly (left frame, $f_r + f_d = 1$). The same properties are shown on the right but fraction of rods is shown for uniaxial field aided runs and fraction of discs—for planar field aided runs.

Resulting fractions of rods and discs, f_r and f_d, are shown in **Figure 8** as functions of N_{ch} for both types of runs. Left frame (unaided self-assembly case) indicates the broad region of the rod-disc coexistence at intermediate values of N_{ch}. At $N_{ch} = 64$ the system approaches symmetric case with both conformations transforming into a spherulitic shape. The right frame contains data for f_r for uniaxial field aided self-assembly and data for f_d for planar field aided self-assembly, therefore, $f_r + f_d \neq 1$ as both are obtained for different conditions. The shapes of both curves are much steeper as compared to the left frame plot indicating the possibility to control the molecular conformation by means of initial field of appropriate symmetry. Therefore, there is some interval of grafting density, where DNPs exhibit rod-disc shape bistability and, hence, the Sm_A-Col morphology bistability is observed in the melt. Spontaneous self-assembly yields the polydomain structure with both Sm_A and Col fragments. Sm_A or Col morphology can be made dominant or, at least, enhanced by an external field of appropriate symmetry [19]. One of such cases is discussed in detail in Section 5. These results reproduce the main trends of the DNPs self-assembly as previously seen experimentally [5, 8, 9, 17, 20].

4.2 Variation in liquid crystalline groups attachment

The model for DNP considered so far, is characterised by a longitudinal attachment of the terminal LC beads (**Figure 1**) and is found to self-assemble into the Sm_A and Col morphologies discussed above. With respect to the applications, the anisotropy in material mechanical properties depends on the spatial arrangement of the DNPs cores, whereas its optical properties—on the orientations of the LC beads. The Sm_A morphology is lamellar with the layers normal **a**, and also optically uniaxial, characterised by the nematic director **n** collinear to **a** (see **Figure 2**). The Col morphology is a supramolecular assembly of columns, where each column is a stack of disc-shape DNPs itself. The arrangement of columns is uniaxial and is described via vector **a**. However, there is no global nematic order of LC beads in this case, as their orientations are distributed radially in a plane perpendicular to **a**, see **Figure 4**. Therefore, optical response of the Col morphology is essentially different from that of the Sm_A one, bearing some analogy in the difference in opto-mechanical applications of the main- and side-chain LC architectures, see e.g. [21].

It is evident from **Figure 4**, that flat radial orientations of the LC beads in Col phase is the result of the energy penalty associated with bending of its host ligands. Lateral attachment of the LC bead, see, **Figure 9**, left frame, is also possible from the view of chemical synthesis [17], and may open up a possibility of greater orientation freedom of the LC beads. In particular, one may expect the optically

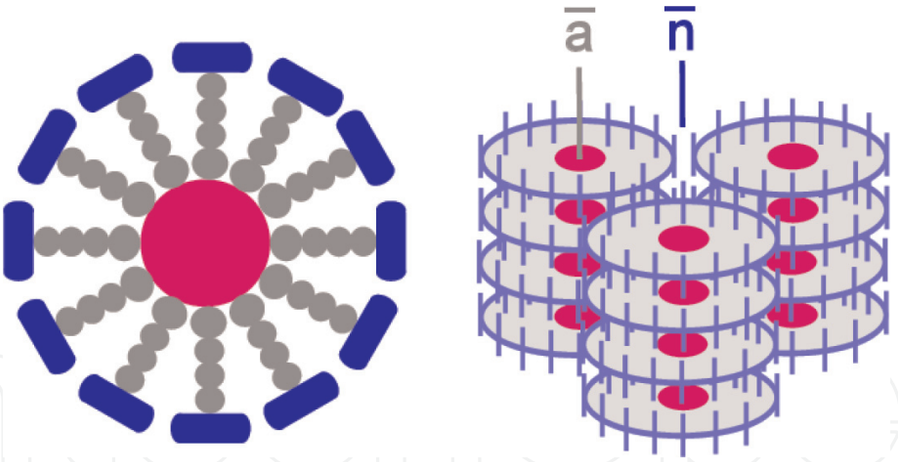

Figure 9.
Model DNP with lateral attachment of LC beads (left frame) and uniaxial Col morphology (right frame).

uniaxial columnar morphology shown in **Figure 9**, right frame, or, some other morphologies as well. With this aim we modified the DNP model accordingly. The orthogonality of LC groups to the spacer-LC bond is maintained by employing two potentials: harmonic bond between the last monomer of the spacer and the centre of the spherocylinder (the bond length is 0.3 nm) and harmonic angular potential between the latter bond and the long axis of the LC bead (equilibrium angle is $\theta_0 = \pi/2$).

Only the case of $N_{\text{ch}} = 32$ ligands is considered and the self-assembly runs are all field-assisted. The field is directed along the Z axis and its magnitude is set at $F = 2 - 4 \cdot 10^{-20}$J. The simulations are performed for the range of pressures $P = 50 - 200$ atm, the duration of each run is 10^6 molecular dynamics steps with a time step of $\Delta t = 20$ fs. For all values of the pressure within this interval the system indeed assemble into the uniaxial hexagonal columnar morphology depicted schematically in **Figure 9** (right frame) and referred thereafter as uCol_h. We use this morphology as an initial state and perform a series of subsequent runs at selected temperatures with the field switched off are aimed on examining the temperature stability of this phase.

For the analysis of the structural changes we consider a number of order parameters. Besides the orientation order parameter S_N (7) we also introduce the hexagonal order parameter $S_H$within the XY plane and columnar order parameter S_C defined as follows

$$S_H = \left\langle \left| \frac{1}{N_k} \sum_{k=1}^{N_k} e^{6j\varphi_k} \right| \right\rangle_{i,t}, \quad S_C = \left\langle \frac{N_{c,i}}{N_{\max}} \right\rangle_{i,t}. \tag{10}$$

Here φ_k is the polar angle of the bond between kth and ith DNPs, where the summation is done over all kth DNPs that belong to a first coordination sphere of ith DNP (see **Figure 10(a)**), $j = \sqrt{-1}$, $N_{c,i}$ is the number of DNPs such as their centres are found inside this cylinder of radius $R_c = 1$nm drawn around the core of the ith DNP along the Z axis (see **Figure 10(b)**), and $N_{\max}$ is the normalisation factor introduced for the sake of convenience.

Evolutions of all order parameters, S_N, S_H and S_C upon the increase of the temperature are shown in **Figure 10**. At low temperatures, $T < 350$ K, the values of all three order parameters are essentially non-zero indicating the uniaxial hexagonal columnar phase uCol_h characterised by uniaxial nematic order, high columnarity and high hexagonal order of the columns. With the increase of the temperature all

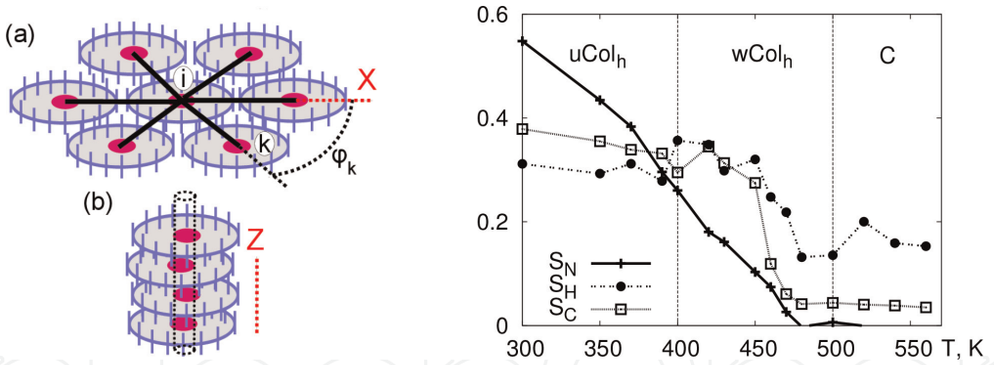

Figure 10.
(a) Flat hexagonal cluster of DNPs and the definition of bond angles φ_k. (b) A column of stacked DNPs. Order parameters S_N, S_H and S_C upon heating the uCol_h.

order parameters gradually decay, but while S_N decays very fast (almost linearly, in contrast with **Figure 6**), the essential delay is observed in the decrease of S_H and S_C. As the result, there is a temperature range around $T = 450$ K, where the value of S_N dropped to about 0.1 (typical for the isotropic phase), but S_H and S_C are still almost the same as in the uCol_h morphology at $T = 300 - 400$ K. This is a columnar morphology with as a weak hexagonal order, wCol_h but still with considerably ordered LC beads. The transition from uCol_h to wCol_h is gradual and the boundary between both shown in **Figure 10** is for rather illustrative purpose. With further heating of the system, all order parameters S_H and S_C drop to their minima at approximately $T \geq 480K$ indicating disordered morphology [22]. Therefore, the simulations predict two novel discotic morphologies for the DNPs with lateral attachment of LC groups: one characterised by an uniaxial, another—by random orientations of the LC groups.

5. Photo-assisted self-assembly for the azobenzene-decorated nanoparticles

Results presented in Sections 3 and 4 indicate that efficient self-assembly of model DNPs into monodomain morphologies faces certain difficulties. These are not the artefacts of the model or the simulation approach, but reflect physical properties of the LC polymers, which are relatively viscous and characterised by slow relaxation and strong tendencies for metastability attributed to the presence of a transient network [23]. One of the ways to stimulate/control the self-assembly of DNPs is to use the light [24–28]. To utilise this approach, the chromophores (e.g. azobenzene, cinnamoyl, diarylethene dithiophenols, etc.) are incorporated into the DNPs ligands. These effects share similarities with photoinduced structural changes in azobenzene-containing side-chain polymers.

Azobenzene chromophore is one of the most widely used, it exists in the trans- and cis-forms. The trans-isomer is prolate and has the LC properties, the cis-one is a non-LC. The photoisomerisation occurs between these forms when illuminated by a light with suitable wavelength. The trans-cis photoisomerization is angle-selective, the reverse one is not. If the absorption bands for both transformations overlap, the continuous trans-cis-trans isomerization cycles take place resulting in the reorientation of the trans-isomers predominantly perpendicularly to the light polarisation axis ('orientation hole-burning' or Weigert effect). Both polarised and unpolarized light can be used to photo-align the trans-isomers. In the latter case, as pointed out by Ikeda [29], 'only the propagation direction is, in principle,

perpendicular to the electric vector of the light. Thus, when unpolarized light is employed, it is expected that the azobenzene moieties become aligned only in the propagation direction of the actinic light'. This situation opens up a possibility for uniaxial alignment of azobenzenes in the direction of the light propagation and is exploited for our model DNPs melt.

We follow Ref. [30] in complementing the deterministic part of the simulations, provided by molecular dynamics, with stochastic part, which describes photoisomerisation of chromophores on a coarse-grained level. We represent trans-isomers via coarse-grained t-beads and their cis-counterparts—by c-beads. Both are considered of the same spherocylinder shape, but t-t interaction is of the LC type (described by a potential (2)), whereas the t-c and c-c interactions are non-LC soft repulsive (described by a potential of the similar form as (1) and (4)). The quantum mechanical nature of photoisomerization [31, 32] is accounted for implicitly, by applying the kinetic equations of a general form for the probabilities of the transitions between the t- and c-state of each ith bead:

$$\begin{cases} p_i(t \to c) = p_t \left(\hat{\mathbf{e}}_i \cdot \hat{\mathbf{i}}\right)^2 \\ p_i(c \to t) = p_c, \end{cases} \tag{11}$$

where $\hat{\mathbf{i}}$ is the unit vector collinear with the light polarisation axis, and p_t and p_c are the respective transition rates that depend on the chemical details of the chromophore group and the intensity and the wavelength of the illumination. The switch of the state is attempted for each chromophore at each MD step. Selective absorption of the light by the azobenzene chromophores is reflected in the angular dependence of the transition probability $p_i(t \to c)$. Photoisomerisation also involves the random change of the chromophore orientation [30, 31]. The choice being made for $p_t = 0.001$ and $p_t/p_c = 0.5$ is justified in detail in [33] and leads to the concentration of c-beads of 5–10% in a photostationary state.

As was discussed in Section 3, the model DNP is found to exhibit rod-disc shape bistability at a wide interval of $N_{\text{ch}} = 24 - 56$ (see, **Figure 8**) resulting in a polydomain mixture of both *SmA* and Col domains upon cooling it down from isotropic state. To avoid this uncertainty we use the DNPs with $N_{\text{ch}} = 12$, in which case only Sm_A morphology is found.

To monitor the level of Sm_A ordering in a system, we consider a set of relevant characteristics. Each DNP is considered in terms of its equivalent ellipsoid provided by the gyration tensor components (8). The asphericity, A, is defined as an average $A = \left\langle (3/2)(\lambda_{\max} + \lambda_{\text{med}} + \lambda_{\min})/R_g^2 - 1/2 \right\rangle$. Orientation order of DNPs is defined as $S_2 = \left\langle P_2\left(\hat{\mathbf{E}} \cdot \hat{\mathbf{N}}\right) \right\rangle$, where $\hat{\mathbf{E}}$ is the orientation of DNP long axis and the nematic director $\hat{\mathbf{N}}$ is evaluated in a way usual for LC. Global smectic order in a system is linked to the level of 'lamellarity' in the arrangement of DNPs cores and is quantified via the amplitude of the density wave along the layer normal. It is evaluated by finding the maximum of the expression

$$S(p) = \max \left| \left\langle e^{i2\pi\left(\mathbf{R}\cdot\hat{\mathbf{N}}\right)/p} \right\rangle \right|, \tag{12}$$

as a function of p (here $i = \sqrt{-1}$). The maximum position $p_{\|}$ provides the pitch of the SmA phase, whereas the smectic order parameter is $S_s = S\left(p_{\|}\right)$. To examine polydomain structure in a system we split it into separate Sm_A clusters (if more than one exist) and calculate their number per molecule, N_c, and the reduced maximum

cluster size M_c, which is the number of DNPs in a largest cluster divided by the total number of DNPs. For the monodomain morphology one has $N_c \to 0$ and $M_c \to 1$, whereas for a highly polydomain phase: $N_c \to 1$ and $M_c \to 0$. The magnitude of all characteristics, A, S_2, S_s, N_c and M_c, are, therefore, restrained to the interval between 0 and 1.

We start from the heating runs. The initial monodomain Sm_A morphology was prepared with the aid of the orienting field (6). The changes in its properties are monitored then in a temperature interval from 400 to 550 K with the field switched off. These changes are shown in **Figure 11**. As follows from there, the system undergoes sharp changes at $T^* \approx 510\,K$: both order parameters S_2 and S_s sharply drop to zero indicating the presence of the order-disorder transition. The synchronicity in the evolution of A, S_2 and S_s indicates the absence of the purely nematic phase (S_2>0 and $S_s = 0$) and a strong relation between the molecular shape and the symmetry of the ordered morphology, similarly to the case discussed in Section 3. Therefore, the transition that occurs at T^* is the Sm_A-I transition. The behaviour of N_c and M_c indicates the monodomain morphology at $T = 400 - 500\,K$ which is transformed into a highly polydomain one in a course of a transition.

We attempt next the reverse transition: a spontaneous self-assembly of the Sm_A morphology out of the isotropic obtained upon cooling down the initial isotropic state. Various cooling rates ranging from 0.37 to 4.5 K/ns are used (note, that because of coarse-graining, the time scale is essentially contracted comparing with the real systems). The results are shown in **Figure 12**. Their behaviour demonstrate that at low enough cooling rate of 0.37 K/ns A, N_c and M_c closely follow their

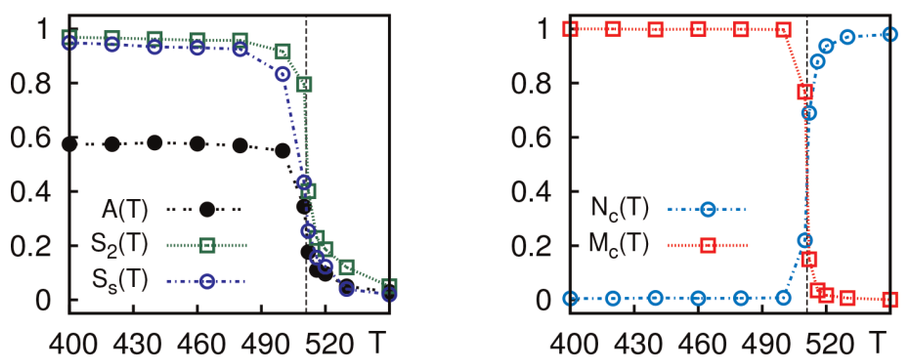

Figure 11.
A, S_2 and S_s (left frame) and N_c and M_c (right frame) vs. T. Initial state: monodomain Sm_A, heated up to T indicated in each plot. Reprinted with permission from [33]. Copyright (2016) American Chemical Society.

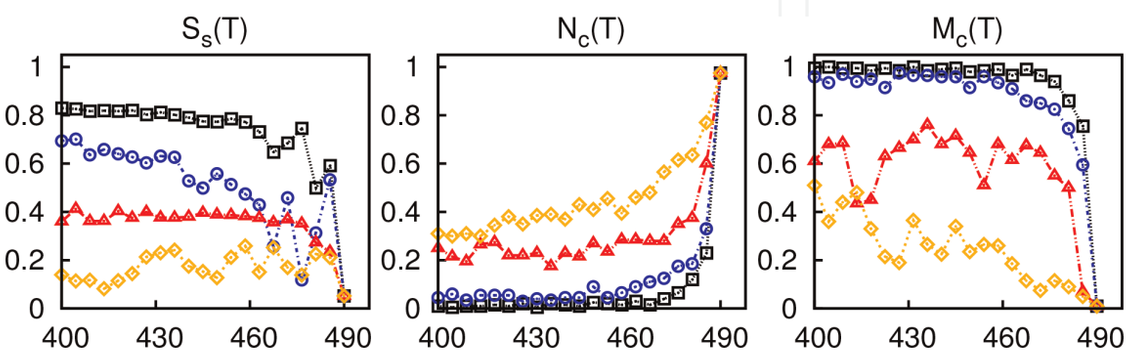

Figure 12.
Temperature dependence of S_s, N_c and M_c. Initial state: isotropic system, cooled down from 490 K to a given T. Cooling rates: Black squares: 0.37 K/ns, blue circles: 0.75 K/ns, red triangles: 1.12 K/ns, and orange diamonds: 4.5 K/ns. No illumination is applied. Adapted with permission from [33]. Copyright (2016) American Chemical Society.

respective curves shown in **Figure 11**. The order parameter S_s do not quite reach its respective value found in **Figure 11** but is, nevertheless, close. At higher cooling rate of 1.12 K/ns the system is trapped in a polydomain state with $N_c \sim 0.2$ (about 40 individual clusters). The maximum cluster size is still quite large, $M_c \sim 0.6$ (about 120 DNPs). This indicates the coexistence of one large and about 40 smaller clusters. At higher cooling rate the system is split into a larger number of smaller clusters, as indicated by N_c and M_c.

To examine the origin of this metastable state, we performed analysis of the translational and rotational mobility of DNPs in a temperature interval of $350 - 500$ K. The system was quenched at each temperature for 30 ns and the initial $1 - 8$ ns of each the run were analysed by splitting it into time blocks at time instances $\{t_k\}$ of equal duration $\delta t = t_k - t_{k-1} = 0.2$ ns. We define instantaneous translational and rotational diffusivities

$$d(t_k) = \frac{1}{6\delta t}\left\langle [\mathbf{R}(t_k) - \mathbf{R}(t_{k-1})]^2 \right\rangle, \quad r(t_k) = \frac{1}{2\delta t}\left\langle \left[\hat{\mathbf{E}}(t_k) \cdot \hat{\mathbf{E}}(t_{k-1})\right]^2 \right\rangle \tag{13}$$

at each t_k, being averaged over initial $1 - 8$ ns, they provide short-time translational $D = \langle d(t_k) \rangle$ and rotational $R = \langle r(t_k) \rangle$ diffusion coefficients of the DNPs at the early stage of a self-assembly. The temperature dependence of both is shown in **Figure 13** as black legends. Both characteristics are high at 500 K and decay sharply as the temperature decreases, indicating a slowdown of translational and rotational mobility of DNPs. Hence, at lower temperatures one observes physically cross-linked domains, similarly to the case of side-chain LC polymers [23]. To quantify orientational arrest of chromophores at lower temperatures we estimated their rotation relaxation time as the function of the temperature from the time autocorrelation function $\langle \hat{\mathbf{e}}(t) \cdot \hat{\mathbf{e}}(0) \rangle$ for their orientations assuming its exponential decay

$$C(t) = \langle \hat{\mathbf{e}}(t) \cdot \hat{\mathbf{e}}(0) \rangle \sim \exp\left[-\frac{t}{t_{\text{rot}}}\right], \tag{14}$$

The evaluation time interval is restricted again to the initial $1 - 8$ ns of each run. The dependence of t_{rot} on temperature shows an essential increase of $1 - 1.5$ order of magnitude upon lowering the temperature from 500 down to 350 K, see **Figure 13**.

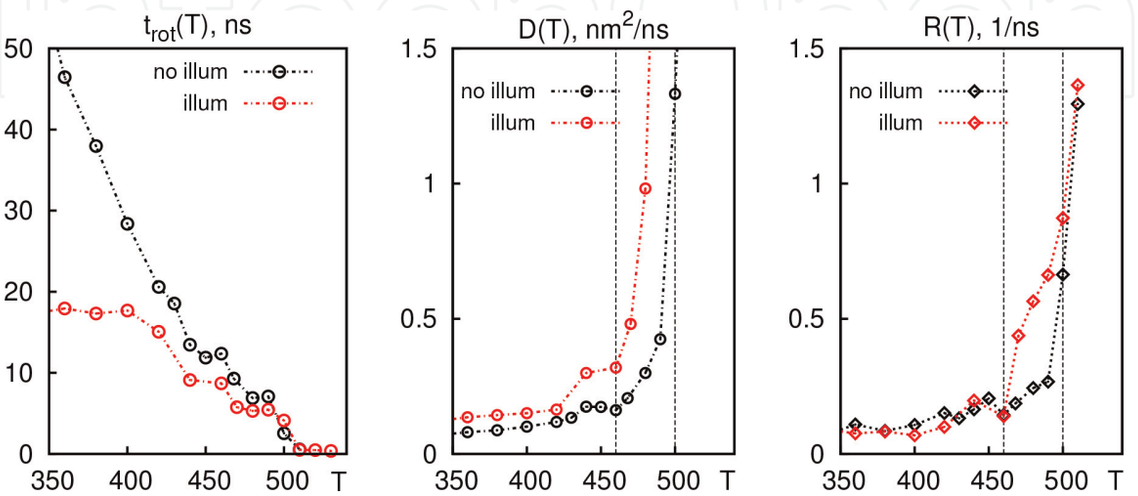

Figure 13.
Chromophores rotation relaxation time t_{rot} and short-time translational D and rotational R diffusion coefficients. Illuminated melt (red legends) vs. non-illuminated melt (black legends). Reprinted with permission from [33]. Copyright (2016) American Chemical Society.

Let us project now the effects of the illumination on the self-assembly of the DNPs. There are two known types of photomodulation in azobenzene-containing systems: (A) weakening (or elimination) of the LC order, and/or (B) order-order transition [29]. The effect (A) should weaken the interdomain links and increasing translation and rotation freedom of the DNPs. This is found in the performed simulations, as is seen from the **Figure 13** (red legends). While the differences between illuminated and no illuminated cases are negligible around 500 K, t_{rot} under illumination decreases by a factor of 2.5 at 350 K. Higher mobility of DNPs under illumination is also detected at higher valued of D and R, especially at 460 – 500 K.

These effects of illumination manifest theirselves on the self-assembly in a course of cooling runs. The results for S_s, N_c and M_c under illumination are shown in **Figure 14**. Similar behaviour is found for most characteristics as compared to the no illumination case, **Figure 12**, but at different respective cooling rates. The illumination reduces the self-assembly time-scale on average by a factor of 3–4 as compared to the no illumination case. Let us note again that the model time-scale is contracted comparing with the real units due to coarse-graining, therefore we emphasise on the relative speed-up of a self-assembly but not on the absolute cooling rates.

To have additional proof on the ability of the illumination to aid self-assembly of DNPs, we performed quenching runs. With no illumination applied, such runs end up in a glassy-like metastable state with no evidence of the orientational or positional order. The situation is markedly different under illumination, as indicated in **Figure 15** for a set of properties A, S_2, S_s, N_c and M_c. Comparing with **Figure 11** for

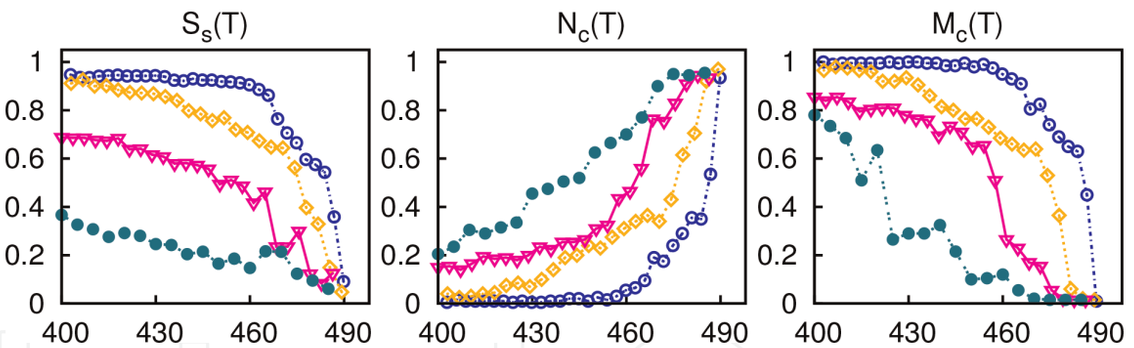

Figure 14.
Temperature dependence of S_s, N_c and M_c. Initial state: isotropic system, cooled down from 490 K to a given T indicated in the plot. Cooling rates: Blue circles: 0.75 K/ns, orange diamonds: 3.75 K/ns, pink triangles: 18 K/ns, green discs: 25 K/ns. The case with illumination. Adapted with permission from [33]. Copyright (2016) American Chemical Society.

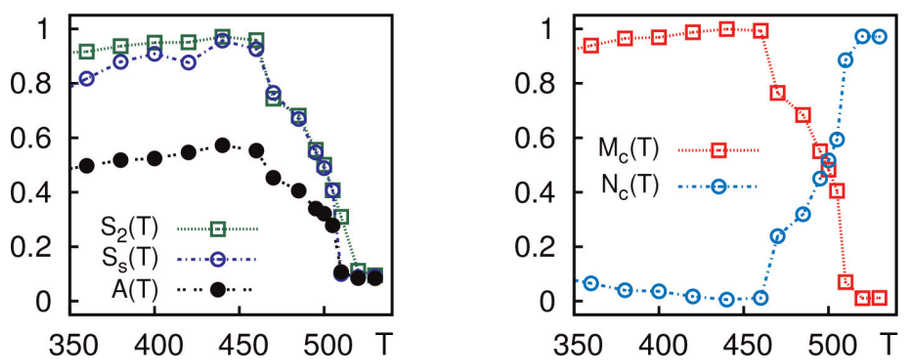

Figure 15.
A, S_2 and S_s (left frame) and N_c and M_c (right frame) vs. T. *Initial state: isotropic system quenched to* T *under illumination. Reprinted with permission from [33]. Copyright (2016) American Chemical Society.*

heating runs, one finds the curves of similar respective shapes albeit all shifted to the lower temperatures. Therefore, computer simulation studies indicate the possibility for the Sm_A phase self-assemble by quenching the system in a broad temperature interval under illumination, otherwise impossible for the non-illuminated system. Although, these simulation findings cannot be compared straightaway with the particular experiments, they are very much in-tune with the general applications of the azobenzene chromophores to control LC alignment, aggregation and self-assembly in the systems of DNPs [24–28].

6. Conclusions

Coarse-grained modelling technique maps chemical details of nanoparticles onto physical set of structure elements. In particular, the dimensions and the type of the core (metal or organic) are examined, the number and the properties of ligands (e.g. flexible or rigid, aliphatic or aromatic, etc.) are analysed, as well as the nature and properties of terminal functional groups (if any). These structure elements are replaced then by classical mechanics objects of appropriate shape that are connected via Hookean springs and interact via van der Waals forces. The parameters of the effective interaction potentials are found from related atomistic simulations using various techniques (e.g. force matching). While lacking chemical specificity of particular type of decorated nanoparticles, such models focused instead on important generic features of a whole class of underlying objects. More importantly, such simplification enables to reach required time- and length-scales of the self-assembly.

In this study we showed that such type of computer simulations is able to reproduce a wide spectra of experimentally observed features related to the self-assembly of decorated nanoparticles. Namely, we demonstrate self-assembly of model nanoparticles into lamellar smectic and columnar morphologies, reproduce and studied the shape-morphology relation, examine preference of ordered phase depending on the decoration density, study temperature driven order-disorder transitions. New optically uniaxial hexagonal phases are predicted for the case of laterally functionalised ligands.

Being viscous fluids, the melts of decorated nanoparticles are prone to slow relaxation and associated with this metastability. This restricts their application where fast regrowing/restructuring of the nanomaterial is needed in response on external stimulus. We demonstrate that the illumination of a suitable choice can be used for the speed-up of the self-assembly of the chromophore-containing nanoparticles.

The work can be extended in a number of ways. First, the use of the more accurately parameterised interaction potentials: if not for predicting the exact phase boundaries for new morphologies, then at least to show a right direction of where to search for them. Second, to consider specific (magnetic or non-metal) nanoparticles. Finally, the use of larger system sizes is always preferable. In conclusion: despite the increase in computing power, the coarse-grained picture always provides a valuable insight on the problem by focusing on its most relevant features.

Acknowledgements

The author thanks M.R. Wilson, J. Lintuvuori, M. Saphiannikova and A. Slyusarchuk for fruitful collaboration on the topic, as well as S. Sokołowski, S. Santer and E. Gorécka for stimulating discussions.

IntechOpen

IntechOpen

Author details

Jaroslav Ilnytskyi
Institute for Condensed Matter Physics, Lviv, Ukraine

*Address all correspondence to: iln@icmp.lviv.ua

IntechOpen

© 2020 The Author(s). Licensee IntechOpen. This chapter is distributed under the terms of the Creative Commons Attribution License (http://creativecommons.org/licenses/by/3.0), which permits unrestricted use, distribution, and reproduction in any medium, provided the original work is properly cited. CC BY

References

[1] Yokoyama M, Hosokawa K, Nogi M, Naito T, editors. Nanoparticle Technology Handbook. Amsterdam: Elsevier; 2008

[2] Hepel M, Zhong C-J, editors. Functional Nanoparticles for Bioanalysis, Nanomedicine, and Bioelectronic Devices. Vol. 1. American Chemical Society; 2012. DOI: 10.1021/bk-2012-1112

[3] Ariga K, Nishikawa M, Mori T, Takeya J, Shrestha LK, Hill JP. Self-assembly as a key player for materials nanoarchitectonics. Science and Technology of Advanced Materials. January 2019;**20**(1): 51-95. DOI: 10.1080/14686996.2018.1553108

[4] Kumar S. Nanoparticles in discotic liquid crystals. In Series in Soft Condensed Matter. World Scientific; October 2016. pp. 461-496. DOI: 10.1142/9789814619264_0013

[5] Draper M, Saez IM, Cowling SJ, Gai P, Heinrich B, Donnio B, et al. Self-assembly and shape morphology of liquid crystalline gold metamaterials. Advanced Functional Materials. Mar 2011;**21**(7):1260-1278. DOI: 10.1002/adfm.201001606

[6] Heinz H, Pramanik C, Heinz O, Ding Y, Mishra RK, Marchon D, et al. Nanoparticle decoration with surfactants: Molecular interactions, assembly, and applications. Surface Science Reports. February 2017;**72**(1): 1-58. DOI: 10.1016/j.surfrep.2017.02.001

[7] Agrawal AK, Kumar K, Swarnakar NK, Kushwah V, Jain S. Liquid crystalline nanoparticles: Rationally designed vehicle to improve stability and therapeutic efficacy of insulin following oral administration. Molecular Pharmaceutics. May 2017; **14**(6):1874-1882. DOI: 10.1021/acs.molpharmaceut.6b01099

[8] Choudhary A, George T, Li G. Conjugation of nanomaterials and nematic liquid crystals for futuristic applications and biosensors. Biosensors. July 2018;**8**(3):69. DOI: 10.3390/bios8030069

[9] Shen Y, Dierking I. Perspectives in liquid-crystal-aided nanotechnology and nanoscience. Applied Sciences. June 2019;**9**(12):2512. DOI: 10.3390/app9122512

[10] Voth GA, editor. Coarse-Graining of Condensed Phase and Biomolecular Systems. CRC Press; 2008. ISBN 1420059556. Available at: https://www.amazon.com/Coarse-Graining-Condensed-Phase-Biomolecular-Systems/dp/1420059556?SubscriptionId=0JYN1NVW651KCA56C102&tag=techkie-20&linkCode=xm2&camp=2025&creative=165953&creativeASIN=1420059556

[11] Rühle V, Junghans C, Lukyanov A, Kremer K, Andrienko D. Versatile object-oriented toolkit for coarse-graining applications. Journal of Chemical Theory and Computation. Dec 2009;**5**(12):3211-3223. DOI: 10.1021/ct900369w

[12] Orlandi S, Zannoni C. Phase organization of mesogen-decorated spherical nanoparticles. Molecular Crystals and Liquid Crystals. May 2013; **573**(1):1-9. DOI: 10.1080/15421406.2012.763213

[13] Baran Ł, Sokolowski S. A comparison of molecular dynamics results for two models of nanoparticles with fixed and mobile ligands in two-dimensions. Applied Surface Science. Feb 2017;**396**:1343-1351. DOI: 10.1016/j.apsusc.2016.11.159

[14] Hughes ZE, Wilson MR, Stimson LM. Coarse-grained simulation studies of a liquid crystal dendrimer: Towards computational predictions of nanoscale structure through microphase separation. Soft Matter. 2005;**1**(6):436. DOI: 10.1039/b511082c

[15] Ilnytskyi J, Lintuvuori J, Wilson MR. Simulation of bulk phases formed by polyphilic liquid crystal dendrimers. Condensed Matter Physics. 2010;**13**(3): 33001. DOI: 10.5488/cmp.13.33001

[16] Lintuvuori JS, Wilson MR. A new anisotropic soft-core model for the simulation of liquid crystal mesophases. The Journal of Chemical Physics. 2008; **128**(4):044906. DOI: 10.1063/1.2825292

[17] Saez IM, Goodby JW. Supermolecular liquid crystals. Journal of Materials Chemistry. 2005;**15**(1):26. DOI: 10.1039/b413416h

[18] Ilnytskyi JM, Neher D. Structure and internal dynamics of a side chain liquid crystalline polymer in various phases by molecular dynamics simulations: A step towards coarse graining. The Journal of Chemical Physics. 2007;**126**(17):174905. DOI: 10.1063/1.2712438

[19] Ilnytskyi J. Relation between the grafting density of liquid crystal macromolecule and the symmetry of self-assembled bulk phase: Coarse-grained molecular dynamics study. Condensed Matter Physics. 2013;**16**(4): 43004. DOI: 10.5488/cmp.16.43004

[20] Gowda A, Kumar S. Recent advances in discotic liquid crystal-assisted nanoparticles. Materials. March 2018;**11**(3):382. DOI: 10.3390/ma11030382

[21] Ikeda T, Mamiya J-i, Yu Y. Photomechanics of liquid-crystalline elastomers and other polymers. Angewandte Chemie, International Edition. Jan 2007;**46**(4):506-528

[22] Slyusarchuk A, Ilnytskyi J. Novel morphologies for laterally decorated metaparticles: Molecular dynamics simulation. Condensed Matter Physics. Dec 2014;**17**(4):44001. DOI: 10.5488/cmp.17.44001

[23] Gallani JL, Hilliou L, Martinoty P, Keller P. Abnormal viscoelastic behavior of side-chain liquid-crystal polymers. Physical Review Letters. Mar 1994; **72**(13):2109-2112. DOI: 10.1103/physrevlett.72.2109

[24] Kuang Z-Y, Fan Y-J, Tao L, Li M-L, Zhao N, Wang P, et al. Alignment control of nematic liquid crystal using gold nanoparticles grafted by the liquid crystalline polymer with azobenzene mesogens as the side chains. ACS Applied Materials & Interfaces. July 2018;**10**(32):27269-27277. DOI: 10.1021/acsami.8b07483

[25] Chu Z, Han Y, Bian T, De S, Král P, Klajn R. Supramolecular control of azobenzene switching on nanoparticles. Journal of the American Chemical Society. Dec 2018;**141**(5):1949-1960. DOI: 10.1021/jacs.8b09638

[26] Biswas TK, Sarkar SM, Yusoff MM, Rahman ML. Synthesis and characterization of azobenzene-based gold nanoparticles for photo-switching properties. Journal of Molecular Liquids. Feb 2016;**214**:231-237. DOI: 10.1016/j.molliq.2015.12.078

[27] Song H, Jing C, Ma W, Xie T, Long Y-T. Reversible photoisomerization of azobenzene molecules on a single gold nanoparticle surface. Chemical Communications. 2016;**52**(14): 2984-2987. DOI: 10.1039/c5cc10468h

[28] Wang Q, Li D, Xiao J, Guo F, Qi L. Reversible self-assembly of gold nanorods mediated by photoswitchable molecular adsorption. Nano Research. April 2019;**12**(7):1563-1569. DOI: 10.1007/s12274-019-2393-9

[29] Ikeda T. Photomodulation of liquid crystal orientations for photonic applications. Journal of Materials Chemistry. 2003;**13**(9):2037. DOI: 10.1039/b306216n

[30] Ilnytskyi JM, Saphiannikova M. Reorientation dynamics of chromophores in photosensitive polymers by means of coarse-grained modeling. ChemPhysChem. Sep 2015; **16**(15):3180-3189. DOI: 10.1002/cphc.201500500

[31] Dumont M, El Osman A. On spontaneous and photoinduced orientational mobility of dye molecules in polymers. Chemical Physics. Jul 1999; **245**(1–3):437-462. DOI: 10.1016/s0301-0104(99)00096-8

[32] Tiberio G, Muccioli L, Berardi R, Zannoni C. How does the trans-cis photoisomerization of azobenzene take place in organic solvents? ChemPhysChem. mar 2010;**11**(5): 1018-1028. DOI: 10.1002/cphc.200900652

[33] Ilnytskyi JM, Slyusarchuk A, Saphiannikova M. Photocontrollable self-assembly of azobenzene-decorated nanoparticles in bulk: Computer simulation study. Macromolecules. Nov 2016;**49**(23):9272-9282. DOI: 10.1021/acs.macromol.6b01871